Lab on a Chip

PAPER

View Article Online
View Journal

Cite this: DOI: 10.1039/d5lc00467e

Centrifugal microfluidic chip with an air gap for oil-free production of enhanced adipogenic multicellular microspheres†

Xueqing Ren,‡ Xin Wang,‡ Xiaolu Cai,‡ Yi Zou, Peng Chen, * Bi-Feng Liu * and Yiwei Li *

Hydrogel microspheres, derived from natural or synthetic materials, serve as crucial platforms for three-dimensional (3D) cell culture and tissue engineering. While traditional production methods like emulsification and microfluidics are widely used, they often involve complex processes and oil phases that can compromise biocompatibility. Here, we present a novel centrifugal microfluidic device with an air gap for producing hydrogel microspheres. Centrifugal force provides a driving force for uniform parallel channels, enabling high-throughput microsphere generation while ensuring size uniformity. The system enables precise size control through centrifugal speed modulation, producing microspheres with diameters ranging from 140.6 ± 17.3 μm to 417.1 ± 34.4 μm with a coefficient of variation below 4.8%. The air gap within the microchannel establishes a step-structure that enables oil-free microsphere generation while ensuring biocompatibility. Moreover, by blending a collagen solution into sodium alginate as the matrix, oil-free microspheres with an interpenetrating polymer network (IPN) can be fabricated, which exhibit excellent biocompatibility to support the culture and adipogenic differentiation of mesenchymal stem cells (MSCs). When cells are cultured with a microsphere-formed scaffold, they exhibit aggregation behavior for enhanced cell–cell communication, which further elevated their adipogenic differentiation potential. Overall, this simplified, high-throughput approach offers a unique platform for applications in cell delivery, drug screening, and tissue engineering.

Received 12th May 2025,
Accepted 14th July 2025

DOI: 10.1039/d5lc00467e

rsc.li/loc

Introduction

Hydrogel microspheres have emerged as versatile platforms for controlled cell delivery and drug release, owing to their high water content, biocompatibility, and structural similarity to the natural extracellular matrix (ECM).[1–4] Various materials have been developed for microsphere fabrication, including sodium alginate,[5,6] agarose,[7] and poly(ethylene glycol) (PEG).[8] Among these, alginate has gained particular attention due to its excellent biocompatibility, biodegradability, and mechanical properties.[9,10] However, to better mimic natural tissue environments, incorporation of key ECM components such as collagen, laminin, and fibronectin is essential. Type I collagen, being the primary ECM component, has been extensively integrated into hydrogel microsphere designs.[11,12]

While existing microsphere production techniques have contributed to the field, each faces inherent constraints that limit broader application. Electrospray methods exhibit high parameter sensitivity, limited production capacity and high equipment requirements.[13,14] Batch emulsification suffers from water–oil interface instability, producing broad size distributions (CV > 10%).[15,16] Conventional microfluidics, though offering better control, are limited to 10^2–10^3 droplets per minute due to serial microsphere formation.[17]

In two-phase emulsification microfluidic systems, oil and surfactants are required for microsphere formation. Both the oil and surfactants can be toxic to encapsulated living organisms or cells. If biomedical applications required prolonged culturing of encapsulated cargos, the oil phase is often required to be removed before the culturing. To minimize residual oil contamination, time-consuming multi-step washes are typically required;[18,19] during this process, even a stronger surfactant, such as PFO, is required to ensure that no residual oil is left to contaminate the microsphere sample. All the processes, as well as the reagents, can significantly compromise cell viability, elevate production costs, and amplify waste management burdens, thereby severely limiting the applicability of microspheres in

Key Laboratory of Molecular Biophysics of MOE and Hubei Bioinformatics & Molecular Imaging Key Laboratory, Department of Biomedical Engineering, College of Life Science and Technology - The Key Laboratory for Biomedical Photonics of MOE at Wuhan National Laboratory for Optoelectronics, Huazhong University of Science and Technology, Wuhan 430074, China. E-mail: gwchenpeng@hust.edu.cn, bfliu@hust.edu.cn, yiweili@hust.edu.cn

† Electronic supplementary information (ESI) available. See DOI: https://doi.org/10.1039/d5lc00467e

‡ These authors contributed equally to this work.

biomedical applications when handling living cargos, such as 3D cell culture, tissue engineering scaffolds, and cell delivery. Therefore, eliminating the oil phase is not merely a process simplification but a critical prerequisite to overcome these fundamental limitations. Centrifugal microfluidics have recently emerged as a highly promising alternative platform owing to their simplicity of operation, cost-effectiveness, and high throughput, which are achieved without the requirement for external pumps. This technology has been applied in various fields, such as droplet generation,[20,21] cell separation,[22,23] digital PCR,[24–27] and immunoassays.[28,29]

In this study, we developed a rapid-prototyping centrifugal microfluidic chip with an air gap for producing interpenetrated network (IPN) microspheres. The system utilizes air as the continuous phase, enabling oil-free production, and simplified purification. Utilizing the crosslinking capability between the alginate and calcium chloride ($CaCl_2$), discrete microspheres are generated. The incorporation of collagen into the resulting alginate microspheres robustly supported the culture and adipogenic differentiation of mesenchymal stem cells (MSCs). Furthermore, comprehensive transcriptomic analysis confirmed that these microspheres significantly accelerated cell spheroid formation and enhanced adipogenic potential.

Materials and methods

Materials

Sodium alginate (S100127) was purchased from Aladdin Industrial Corporation. Calcium chloride ($CaCl_2$) was purchased from Shanghai Hushi Laboratorial Equipment Corporation (10005861). Tween-20 was obtained from Biofroxx (1247). Rat tail collagen-I (354236) and Matrigel (356231) were purchased from Corning. Latex beads, carboxylate-modified polystyrene (L5530), were purchased from Sigma. Cell viability was evaluated using a Calcein/PI (C2015M) staining kit (Beyotime Biotechnology). Lipid droplets and nuclei were stained with Nile red (N815046, Macklin), Oil red O (O8010, Solarbio) and Hoechst 33258 (C1011, Beyotime Biotechnology). Cells were induced to differentiate using IBMX (I5879, Sigma), dexamethasone (D1756, Sigma), and insulin (P3376, Beyotime Biotechnology).

Preparation of centrifugal microfluidic chips

The chambers and microchannels of PMMA and PDMS components were designed using AutoCAD software or SolidWorks software. The PMMA chip was produced using CO_2 laser cutting. The bonding between the chip layers was carried out using a pressure-sensitive adhesive. By hot pressing equipment (Hengwei Precision Technology, China) at 50 °C for 10 minutes, the chip layers were directly bonded. The PDMS mold was fabricated following the standard soft lithography method. SU-8 3025 was coated onto a silicon wafer (Dow Corning Corporation, Ml, USA) as the positive master mold of the channel. Polydimethylsiloxane (PDMS, Sylgard184, Dow Corning Corporation) was mixed in a 1 : 10 ratio of the curing agent to elastomer and subsequently degassed and poured onto the SU-8-on-Si wafer master. The PDMS mold was peeled off and cut into 5 × 10 mm pieces attached to a glass slide 5.3 × 10.3 mm after oxygen plasma treatment. The PDMS and PMMA components were filled with a viscous UV-curing adhesive (D-3322, Kafuts, China) and underwent UV curing soon after laying.

Alginate preparation

The sodium alginate purchased from Aladdin was dissolved in deionized water with constant stirring for several hours. The obtained solution was dialyzed in deionized water for 3 days using a membrane with a molecular cut-off weight of 3500 Da. The sterile solution was firstly acquired from a filtration step (0.22 μm) and then lyophilized. The target product of alginate was obtained by sterile reconstitution in a ddH_2O medium at 2.5% (w/v). All sodium alginate solutions with varying concentrations were systematically prepared through serial dilutions from this stock solution (2.5%) using sterile ddH_2O as the diluent.

Production of hydrogel microspheres

The chip can be reused after being cleaned between every experiment. For cleaning, the chip was first ultrasonically cleaned in pure water for 2 hours, with the water replaced every 30 minutes to remove any potential surface contaminants. During ultrasonic cleaning, the water temperature was maintained at 25 °C and the ultrasonic frequency was set to 40 kHz. Subsequently, the chip was dried using a nitrogen gun and then exposed to UV light for 30 minutes to sterilize the surface. 10× PBS buffer, 1 M NaOH and ddH_2O were used to adjust the pH value of collagen-I to 7.4. Sodium alginate with or without collagen solution was added into the chip sample chamber. The hydrogel microspheres in this study consisted of 1.5 mg mL^{-1} rat-tail collagen-I and 10 mg mL^{-1} alginate. The collection chamber was filled with 15 mM $CaCl_2$ with 0.1% Tween-20 solution. After centrifugation, the hydrogel microspheres were sucked out of the collection chamber.

Hydrogel microsphere size characterization

To produce microspheres as described above, 0.5 μm fluorescent beads were added to a mixture of sodium alginate. Centrifuged at different rotational speeds, the hydrogel microspheres were collected. Hydrogel microspheres were imaged with an Olympus spinning disk confocal microscope (CSUW1-T1S), processed using ImageJ (**https://imagej.en.softonic.com/**).

CFD simulation

All simulations were performed using ANSYS Fluent (ANSYS, Inc., PA, USA). To reduce computational cost, one-half of the total domain was employed as the computational domain. The mesh comprised approximately 400 000 *ortho*-hexahedral

elements to ensure numerical accuracy. A pressure-based, double-precision solver was used to simulate the transient process. The volume of fluid and laminar models were adopted to analyze microsphere generation, with velocity-inlet boundary conditions and pressure-outlet boundary conditions. Gravitational acceleration was applied in the *y*-direction to mimic centrifugal acceleration. The contact angles of all walls were set to 180° to approximate ideal conditions. The SIMPLE scheme was used for pressure–velocity coupling. The fluid domain was initialized with air, and half of the microchannel was patched with the fluid to initiate the calculation.

Cell culture

Male C57BL/6J mice were obtained from Guangdong Provincial Medical Laboratory Animal Center. The research protocol involving these animals was approved by the Animal Experimentation Ethics Committee of Sun Yat-sen University and adhered strictly to institutional guidelines concerning the humane treatment of laboratory animals (Approval No. 2023-B027). MSCs were isolated from the adipose tissue of male C57BL/6J mice about 6 weeks. In brief, the adipose tissue was washed three times with phosphate buffered saline, finely minced, and digested with a solution containing 1.25% (w/v) collagenase type I and 4.0% (w/v) bovine serum albumin in DMEM for 30 minutes at 37 °C. The digestion reaction was neutralized with complete culture media that contained Dulbecco's modified Eagle medium: Nutrient Mixture F-12, 10% fetal bovine serum, and 100 units per milliliter antimycotic/antibiotic. The digested tissue was filtered, centrifuged, and resuspended in complete culture media. Finally, the cells were inoculated into the culture bottle, and the medium changed regularly until the cells were subcultured at 70–80% confluence. To passage the cells, 0.25% trypsin–EDTA solution was used. For cell encapsulation culture, the matrix was mixed with the microspheres and cell suspension and then the mixed solutions were immediately deposited onto a 24-well plate. To form cell spheroids, the microspheres were directly mixed with the cell suspension, and then the mixed solutions were immediately deposited onto the 24-well plate.

Adipogenic differentiation

To induce differentiation of MSCs, the growth medium was replaced with medium I containing 10% fetal bovine serum, 100 units per mL penicillin/streptomycin, 0.5 mM IBMX (Sigma), 10 μg mL^{-1} insulin (Beyotime Biotechnology), and 25 μM dexamethasone for 2 days. After this, medium I was replaced with medium II containing 10% fetal bovine serum, 100 units per mL penicillin/streptomycin, and 10 μg mL^{-1} insulin (Beyotime Biotechnology) for 10 days, cycling every 2 days. For adipogenic induction evaluation, cells were stained with Nile red (Macklin) and Oil red O (Solarbio) following the manufacturer's instructions after adipogenic induction.

Cell viability characterization

Calcein AM and PI were employed to characterize cell viability, which was performed on day 3 and day 7 after MSC encapsulation in the matrix and microspheres or directly mixed with microspheres. The cells were imaged using an Olympus spinning disk confocal microscope (CSUW1-T1S), processed using ImageJ (**https://imagej.en.softonic.com/**).

RNA isolation and RT-qPCR

For RT-qPCR, approximately 1×10^6 cells per sample were lysed in 1 ml TRIzol reagent (Invitrogen), the total RNA was extracted according to the manufacturer's instructions, 1 μg RNA was used to synthesize cDNA in a 20 μL total volume using the all-in-one RT SuperMix perfect for qPCR (Vazyme R333-01), and qPCR reactions used 2 μL cDNA per 10 μL SYBR Green master mix (Vazyme Q712-02) and analyzed using the Applied Biosystems™ QuantStudio™ 3 & 5. All procedures were performed in accordance with the manufacturer's instructions. The value for each gene was normalized to that of the reference gene, GAPDH, and the relative expression was calculated by the comparative C_t method ($\Delta\Delta C_t$). The primer sequences were as follows: Fabp4 (forward 5′-AAGGTGAAGAGCATCATAACCCT-3′ and reverse 5′-TCACGCCTTTCATAACACATTCC-3′); Pparg (forward 5′-GGAA GACCACTCGCATTCCTT-3′ and reverse 5′-GTAATCAGCAACCA TTGGGTCA-3′); Adipoq (forward 5′-TGTTCCTCTTAATCCTGCC CA-3′ and reverse 5′-CCAACCTGCACAAGTTCCCTT-3′); GAPDH (forward 5′-AGGTCGGTGTGAACGGATTTG-3′ and reverse 5′-TGTAGACCATGTAGTTGAGGTCA-3′).

Transcriptome sequencing and analysis

For cell samples, approximately 1×10^6 cells per sample were lysed in 1 mL of TRIzol reagent. For adipose tissue samples, approximately 100 mg of tissue was flash-frozen in liquid nitrogen, pulverized into powder, and lysed in 1 mL of TRIzol reagent per sample. Total RNA was extracted according to the manufacturer's protocol. The RNA concentration was quantified using a Qubit 2.0 fluorometer. RNA samples mixed with a loading dye were electrophoresed on a 1.5% agarose gel at 150 V for 20 min. Post-run, gels were visualized under UV and assessed for RNA integrity (sharp 28S/18S rRNA bands) and the absence of genomic DNA contamination (Fig. S1†). The processes of mRNA library construction included mRNA purification and fragmentation, double-stranded cDNA synthesis, purification of double-stranded cDNA, end repair/dA-tailing, adapter ligation, size selection, and library amplification. After quality assessment, the sequencing library suitable for the Illumina platform was obtained. Differential gene functions were annotated *via* KEGG (Kyoto Encyclopedia of Genes and Genomes) pathway analysis. R language (**https://www.r-project.org/**) was used to draw all heatmaps.

Statistical analyses

Data are shown as the mean ± standard deviation (SD). Student's *t*-test was used for comparisons between the two groups. Statistical analysis and graphs were generated using GraphPad Prism software. $*p < 0.05$, $**p < 0.01$, and $***p < 0.001$, respectively.

Results

Design and assembly of the centrifugal microfluidic chip

We developed a multilayer centrifugal microfluidic device for producing IPN microspheres through a systematic design approach. The device architecture comprises five precisely engineered layers, which were integrated using a combination of double-sided pressure-sensitive adhesive (PSA) bonding and thermal pressing techniques to ensure robust sealing (Fig. 1a). A critical component of this microfluidic device is the PDMS-glass microchannel assembly: a PDMS (5 × 10 mm) module featuring parallel two-dimensional microchannels, and this PDMS structure was permanently bonded to a glass substrate (5.3 × 10.3 mm) through oxygen plasma treatment, followed by integration with the PSA interlayer (Fig. 1b). All air-exposed interfaces were sealed using the UV-curable adhesive to prevent fluid leakage. The selective adhesive bonding strategy ensures that the alginate solution can only flow exclusively through the designated microchannel pathway into the microsphere collection chamber, where controlled microsphere formation occurs.

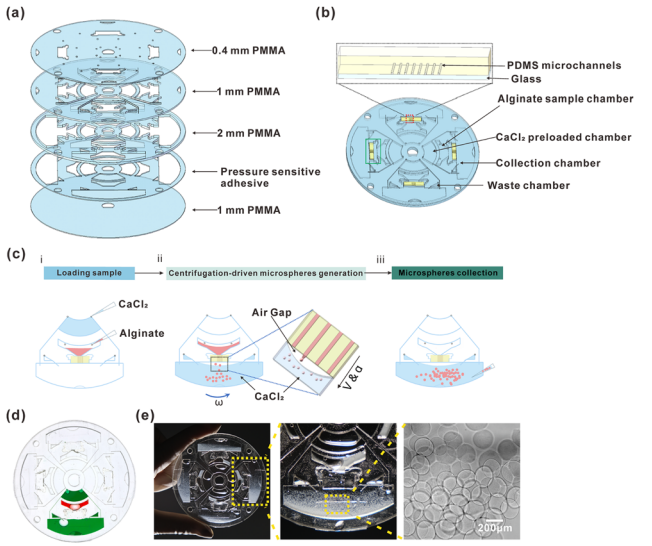

Fig. 1 Engineering design and operational mechanisms of the multilayer centrifugal microfluidic device. (a) Exploded cross-sectional diagram detailing the layer composition (bottom to top): 1 mm PMMA substrate layer, double-sided pressure-sensitive adhesive (PSA) layer, 2 mm PMMA layer, 1 mm PMMA layer, and 0.4 mm PMMA layer. (b) Top-view schematic highlighting the layout of four parallel functional units. Each unit comprises: the alginate sample chamber, PDMS-glass microchannel assembly, $CaCl_2$ preloaded chamber, waste chamber and collection chamber. UV-adhesive bonding points indicated by green markers. (c) Operational sequence demonstrating the microsphere generation mechanism: (i) initial loading of solutions, (ii) centrifugal force-driven flow through microchannels, microsphere formation at channel outlets through surface tension and centrifugal force balance, (iii) microspheres were subjected to gelation and collection (d) photograph of the packaged chip, which has been injected with the pigment. (e) Microspheres accumulated in the $CaCl_2$ solution storage chamber after centrifugation.

Before centrifugation, alginate and $CaCl_2$ solution were initially injected into the alginate sample chamber and $CaCl_2$ preloaded chamber. During centrifugation, the applied centrifugal force causes the $CaCl_2$ solution in the preloaded chamber to redistribute radially outward into the collection chamber, deforming a liquid interface. Simultaneously, the vent holes of the waste chamber positioned at a specific radial distance allowed most of the air in the collection chamber to flow into the atmosphere, leaving a space above the deformed liquid interface that established a critical air gap between the microchannel outlet and the $CaCl_2$ solution surface (indicated in Fig. S2†). Centrifugal force drives the alginate solution through the microchannel into the air gap, where microspheres form at the channel outlet through the balanced interplay of centrifugal force and the surface tension. The gap distance remains stable during operation as excess $CaCl_2$ solution is continuously expelled through the vent hole, maintaining consistent microsphere formation conditions throughout. Then, the microspheres were driven through the air gap and made to come in contact with the crosslinking solution, eliminating premature gelation and ensuring uniform microsphere morphology (Fig. 1c).

As shown in Fig. 1d, the fabricated chip clearly demonstrates the functional partitioning of chambers: green color-coded compartments correspond to $CaCl_2$ solution chambers, while red-labeled modules represent alginate solution chambers. Following centrifugal actuation, the microspheres generated through the microfluidic channels undergo interfacial crosslinking with $CaCl_2$ solution contained within the subjacent chamber, where they are subsequently retained for storage (Fig. 1e).

In our previous work, we developed a rapid prototyping and customized assembled centrifugal step emulsifier (CASE) for high-throughput microsphere generation.[30] However, the

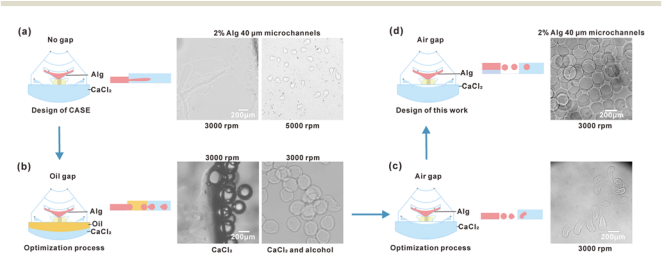

Fig. 2 Diagram of the chip optimization process. (a) Schematic diagram of the no air gap design in the CASE. (b) Schematic diagram of the oil-gap chip. (c) Schematic diagram of the air-gap chip with channels adhering to the bottommost layer structure and the (d) schematic diagram of the air-gap chip with elevated channels detached from the bottommost layer structure.

microsphere collection process necessitates additional washing steps to remove the residual oil phase, which compromises the cytocompatibility of the microspheres. To eliminate this requirement, we re-engineered the CASE for an all-aqueous microsphere generation chip. Here, we outline the steps taken to optimize the CASE for the development of an all-aqueous-phase microsphere generation chip, as shown in Fig. 2.

Initially, we modified our original "no-gap" emulsifier by replacing the oil phase with $CaCl_2$ aqueous solution. At low rotational speeds, filamentous structures were observed during microsphere formation, while higher speeds resulted in tailed microsphere morphologies (Fig. 2a). We hypothesize that these deformations stemmed from premature contact between nascent liquid microspheres and the $CaCl_2$ solution. Subsequently, we introduced an oil phase to create an oil-gap architecture between the water phase microchannel and the $CaCl_2$ solution chamber, anticipating microsphere formation in the oil phase. However, experimental results revealed significant interfacial resistance at the oil–water interface, impeding microsphere formation (Fig. 2b). Even with ethanol supplementation to mitigate surface tension, most obtained microspheres still exhibited substantial deformation. Furthermore, we implemented an air-gap structure to replace the oil gap in the device, and we successfully generated hydrogel microspheres at high speed. However, we still face a challenge where the microspheres can wet the surface of the PMMA bottom, resulting in a non-spherical structure (Fig. 2c). The last improvement is to lift the water phase microchannels, which makes the microspheres flow through the air without any physical contact with the bottom PMMA substrate (Fig. 2d); this feature guaranteed that there is no wetting-induced deformation of microspheres before solidification in $CaCl_2$ solution (Fig. 2d). In conclusion, as compared to our previously published emulsifier, the air-gap design not only prevents the usage of the oil phase and downstream wash steps, but also enables formation of monodisperse hydrogel microspheres.

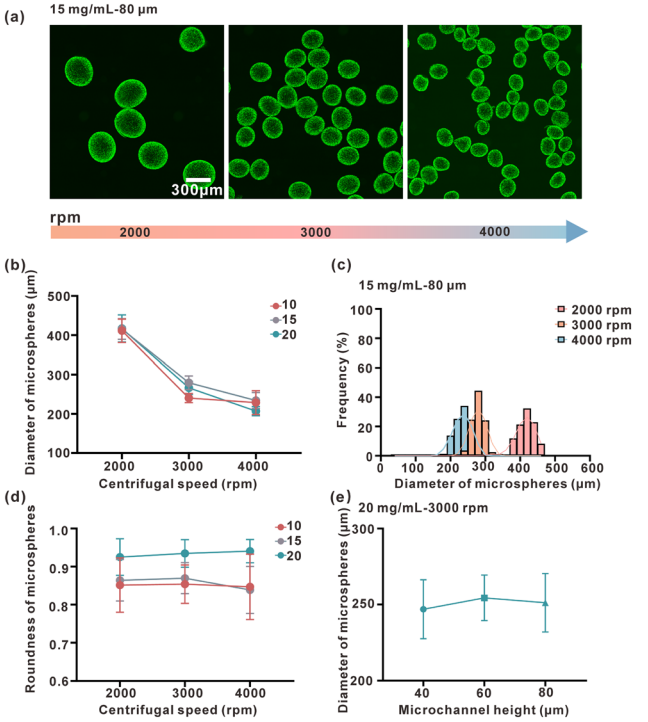

Fig. 3 Optimization of process parameters and characterization of microsphere properties. (a) Fluorescence micrographs showing the microsphere morphology at varying centrifugal speeds: 2000 rpm (415.619 ± 26.307 μm), 3000 rpm (279.149 ± 17.351 μm), and 4000 rpm (234.184 ± 20.263 μm). FITC-labeled 0.5 μm tracer beads used for visualization. (b) Systematic analysis of microsphere diameter variation with the alginate concentration: 10 mg mL^{-1}, 15 mg mL^{-1}, and 20 mg mL^{-1} at 2000, 3000, and 4000 rpm ($n \geq 205$). (c) Quantitative relationship between the centrifugal speed and resultant microsphere diameter, demonstrating an inverse correlation ($n \geq 245$). (d) Systematic analysis of microsphere roundness variation with alginate concentration: 10 mg mL^{-1}, 15 mg mL^{-1}, and 20 mg mL^{-1} at 2000, 3000, and 4000 rpm ($n \geq 205$). (e) Systematic analysis of microsphere diameter variation with microchannel height: 40 μm (246.619 ± 19.431 μm), 60 μm (254.334 ± 14.982 μm), and 80 μm (251.109 ± 19.21 μm) at 3000 rpm ($n \geq 93$).

Optimization of the centrifugal speed, sodium alginate concentration and microchannel height for microsphere formation

We conducted a comprehensive investigation of the impacts of the sodium alginate concentration, centrifugal parameters, and microchannel height, respectively, on the structure of produced microspheres. And the standardized quantification with 20 μL sodium alginate aliquots yielded ~1700 (3000 rpm) microspheres, resulting in agreement between theoretical and actual microsphere yields, confirming the chip's robust production performance (Fig. S3†). The results demonstrate that centrifugal speed emerged as a critical parameter significantly influencing the microsphere size. Using an 80 μm-width channel as the standard condition, we observed that, at 2000 rpm, microspheres exhibited a diameter of 415.619 ± 26.307 μm. Increasing the speed to 3000 rpm resulted in a reduced diameter of 279.149 ± 17.351 μm. Further acceleration to 4000 rpm produced even smaller microspheres 234.184 ± 20.263 μm (Fig. 3a–c).

While alginate concentrations of 10–20 mg mL^{-1} indeed had a minimal impact on the microsphere diameter, there was a notable improvement in the sphericity at the 20 mg mL^{-1} concentration. Specifically, microspheres produced with 20 mg mL^{-1} alginate consistently exhibited roundness values approaching 0.92–0.94, compared to 0.83–0.87 for lower concentrations (Fig. 3d). This enhanced sphericity at higher alginate concentrations can be attributed to increased solution viscosity, which provides better microsphere stability during the formation process and reduces deformation prior to crosslinking. The higher polymer concentration creates stronger intermolecular interactions that help maintain spherical geometry against centrifugal and surface tension forces. Under this condition, we further increased the centrifugal speed, and the diameter of the microspheres was

further reduced to 178.229 ± 9.550 μm (5000 rpm), 140.601 ± 17.339 μm (6000 rpm), as shown in the Fig. S4.†

Our systematic analysis also revealed that the width of the microchannel between 40 and 80 μm had a minimal impact on the final microsphere diameter. Specifically, at a constant centrifugal speed of 3000 rpm, microspheres exhibited diameters of 246.619 ± 19.431 μm, 254.334 ± 14.982 μm, and 251.109 ± 19.216 μm for channel widths of 40 μm, 60 μm, and 80 μm, respectively (Fig. 3e). The microspheres produced using our system consistently demonstrated well-defined shapes and narrow size distributions, with a coefficient of variation below 4.8%. Previous studies have established that microspheres with diameters between 100 and 400 μm generally exhibit optimal performance for cell culture applications,[31] with microspheres around 200 μm showing particularly favorable cell adhesion and proliferation characteristics.[32–34] Based on these considerations, we selected 3000 rpm as our standard operating condition, producing microspheres with a diameter of 200 to 300 μm for subsequent biological validation studies.

We performed further studies to examine whether the ramp-up phase (from rest to the target centrifugal speed) during centrifugation affects the uniformity of microspheres. Owing to the rapid acceleration capability (~6000 rpm s^{-1}) of our custom centrifuge, the target speed of 3000 rpm is achieved within 0.5 s. During this acceleration period, the relationship between the liquid flow velocity and time in our device is shown in Fig. S5.† Within this period, only a volume of 3.49×10^{-5} μL of the liquid was driven into the collection chamber, which yielded approximately 4 microspheres. The proportion of these off-spec microspheres is below 0.04% of the whole population of microspheres, given ~10 000 microspheres were generated by a single run with 110 μL alginate. For calculation of the coefficient of variation, the samples were randomly selected from all the microspheres, during which these off-spec microspheres haven't been excluded.

To investigate the potential impact of sodium alginate pressure reduction during centrifugation on microsphere dimensions, we employed computational fluid dynamics (CFD) simulation to simulate the microsphere formation and evolution processes within microchannels that is challenging to be directly observed.[35–37] The geometry and liquid parameters applied in the simulation are summarized in (Table S1, ESI†) enabling the quantification of size variations under multiple conditions before and after pressure changes. The pressures were calculated using the conditions with either a full-filled water phase in the chamber before microsphere generation or an empty water phase chamber after microsphere generation. The variable pressure should be between the numbers of these two conditions. As a result of CFD simulations, we confirmed the variable pressure and flow rate with different amounts of liquid in the water phase chamber. However, with the same centrifugal speed, which determined the same centrifugal force, we obtained consistent microsphere sizes (Fig. S6†).

Cell encapsulation culture and adipogenic differentiation

To evaluate the biological functionality of our hydrogel microspheres, we conducted detailed cell culture and differentiation studies using mesenchymal stem cells (MSCs). The cells were encapsulated within the alginate and collagen hydrogel microspheres and cultured within a matrix to provide a supportive three-dimensional environment. Time-course microscopy analysis revealed progressive cell–material interactions, with cells demonstrating initial surface attachment by day 3 and achieving extensive surface coverage by day 7. To quantitatively assess cell viability, we performed live/dead staining at these time points. The results demonstrated excellent cell survival, with viability reaching approximately 90% by day 7 (Fig. 4a and b). These findings

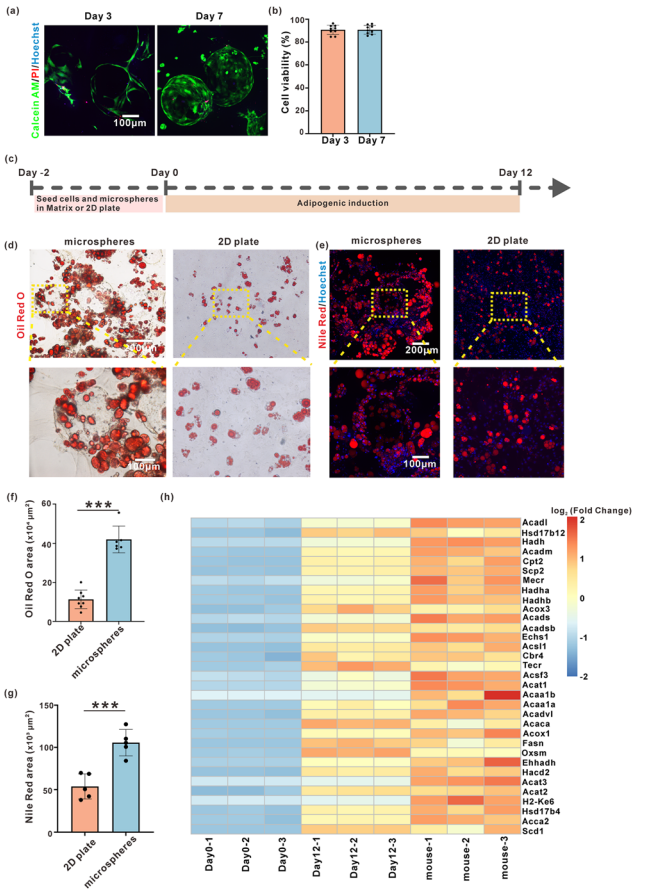

Fig. 4 Quantitative assessment of microsphere-supported adipogenic differentiation. (a) Triple-channel fluorescence imaging of encapsulated MSCs on days 3 and 7 post-encapsulation. Live cells and dead cells. (b) Time-course analysis of cell viability calculated as (Calcein AM-positive area)/(total stained area) × 100% (n = 9). (c) Timeline schematic detailing the differentiation protocol: cell seeding, induction and analysis timepoints. (d) Brightfield microscopy of Oil red O staining comparing lipid accumulation in 2D *versus* microsphere cultures after 12 day induction. (e) Fluorescence imaging of Nile red-stained cultures showing lipid droplet distribution. (f) Quantitative analysis of the Oil red O staining lipid area ($n \geq 6$). (g) Comparative analysis of the Nile red fluorescence staining lipid area (n = 5). (h) RNA-seq derived heatmap showing differential expression of fatty acid metabolism genes.

confirm that our oil-free microsphere production method yields highly biocompatible scaffolds suitable for long-term cell culture applications.[38]

Following the demonstration of high biocompatibility, we investigated the capacity of our microspheres to support adipogenic differentiation of MSCs (Fig. 4c). After a 12 day adipogenic induction period, we conducted a comparative analysis of lipid accumulation between cells cultured on conventional 2D plates and cells growing on the microspheres (Fig. 4d and e). Quantitative analysis using both Oil red O and Nile red staining revealed significantly enhanced lipid accumulation in microsphere cultures. Specifically, oil red O staining showed an approximately 3-fold higher lipid area, while Nile red fluorescence demonstrated a 2-fold increase in cells cultured on microspheres compared to conventional 2D cultures (Fig. 4f and g).

To gain deeper molecular insights into the adipogenic differentiation process, we performed comprehensive transcriptome sequencing comparing three experimental conditions: non-induced MSCs with microspheres, induced mature MSCs with microspheres, and mature adipose tissue from mice. KEGG pathway enrichment analysis revealed that differentially expressed genes were predominantly enriched in fatty acid metabolism pathways. Key genes showing significant regulation included Acadl, Hsd17b12, Hadh, Acadm, Cpt2, Scp2, and others (Fig. 4h).[39,40] Notably, the gene expression profiles of microsphere-induced adipocytes showed remarkable similarity to mature adipose tissue, particularly in pathways related to fatty acid metabolism. These molecular findings provide strong evidence that our hydrogel microspheres not only support cell survival but also maintain and enhance the differentiation potential of MSCs.

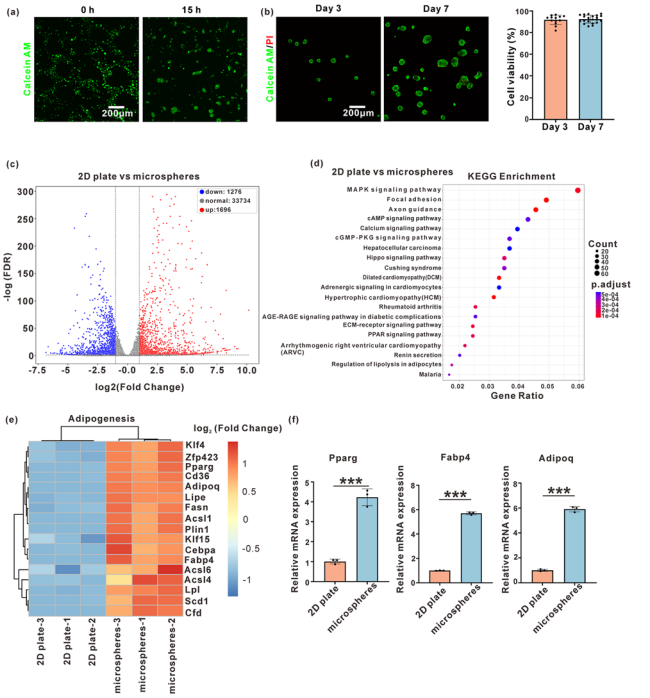

Fig. 5 Microsphere-mediated cellular spheroid and comprehensive molecular characterization of spheroid formation and adipogenic enhancement. (a) Images of the process of microsphere-mediated cellular spheroid formation and (b) time-course analysis of cell viability calculated as (Calcein AM-positive area)/(total stained area) × 100% ($n \geq 13$). (c) Volcano plot analysis of RNA-sequencing data comparing spheroid *versus* 2D cultures at day 6 ($n = 3$). Red dots: upregulated genes (1696 genes, $\log_2FC > 1$, $p < 0.05$); blue dots: downregulated genes (1276 genes, $\log_2FC < -1$, $p < 0.05$); grey dots: non-significant changes. (d) KEGG pathway enrichment analysis visualized as bubble plot. Top enriched pathways: ECM–receptor signaling pathway, Hippo signaling pathway, PPAR signaling pathway, and regulation of lipolysis in adipocytes. (e) Heatmap showing the differential expression of adipogenesis-associated genes between 2D and spheroid cultures. (f) RT-qPCR validation of key adipogenic markers (Pparg, Fabp4, Adipoq) in 2D *versus* spheroid cultures ($n = 3$).

High-throughput cell spheroid formation and enhanced differentiation potential

In addition to our encapsulation studies, we explored an alternative culture configuration where MSCs were directly mixed with the hydrogel microspheres. Intriguingly, we observed that upon contact with the microsphere surfaces, cells underwent a distinct behavioral sequence: initial surface attachment and spreading, followed by progressive aggregation leading to the formation of dense cellular spheroids (Fig. 5a). To quantitatively evaluate cellular viability, live/dead staining assays were conducted at predetermined intervals. The experimental data exhibited exceptional cell survival rates, attaining approximately 90% viability by the seventh day (Fig. 5b). These outcomes confirm that the oil-free methodology for microsphere fabrication produces scaffolds of superior biocompatibility, demonstrating suitability for prolonged multicellular microspheroid culture applications.

To understand the molecular basis of this spheroid formation process and its biological implications, we performed detailed transcriptome analysis comparing spheroid cultures with conventional 2D cultures after 6 days. This analysis revealed substantial transcriptional remodeling, with 1696 genes showing upregulation and 1276 genes showing downregulation in spheroid cultures (Fig. 5c). The biological significance of these expression changes was further investigated through pathway analysis, which revealed significant enrichment in several key signaling networks, the ECM–receptor signaling pathway, Hippo signaling pathway, PPAR signaling pathway, and Regulation of lipolysis in adipocytes (Fig. 5d).

Detailed examination of the adipogenesis-related gene expression revealed that key markers promoting adipogenic differentiation, including Plin1, Adipoq, and Fabp4 showed significant upregulation in spheroid cultures as compared to traditional 2D cultures (Fig. 5e). To validate these transcriptomic findings, we performed targeted RT-qPCR analysis, which confirmed the elevated expression of critical adipogenic regulators including Pparg, Fabp4, and Adipoq (Fig. 5f). These results strongly suggest that the multicellular

spheroids formed through the interaction with our hydrogel microspheres possess enhanced adipogenic potential.[41,42]

The microsphere-induced spheroid formation represents an important advancement in tissue engineering approaches. Mesenchymal cells typically exhibit characteristic properties of isolated spreading, proliferation, and migration; however, their spontaneous aggregation implies a transition toward more epithelial-like characteristics, with reduced migration and enhanced cell–cell adhesion. Our transcriptomic analysis reveals that the microsphere-induced spheroid formation process facilitates this transition, promoting a more tissue-like cellular organization that enhances differentiation potential.

Discussion

In this study, we have successfully developed a centrifugal microfluidic platform for the oil-free production of collagen–sodium alginate IPN hydrogel microspheres. The system's technical innovations and advantages merit detailed consideration. First, our design integrates multiple parallel production units within a single chip, achieving efficient microsphere generation while maintaining remarkable size uniformity (CV $<$ 4.8%). The use of precisely engineered PDMS microchannels (40–80 μm) coupled with controlled centrifugal forces (2000–6000 rpm) enables fine-tuned control over the microsphere's diameter (140–417 μm). This size tunability—achievable through parameter adjustment without chip redesign—enhances flexibility for diverse applications such as tumor spheroids and stem cell aggregates. Notably, the elimination of oil phases not only simplifies the production process but also enhances biocompatibility, as demonstrated by sustained cell viability exceeding 90%.

From a fabrication perspective, our system offers several technical advantages. The multilayer design, incorporating glass, PMMA, and PDMS components, provides both structural stability and precise fluidic control. The selective adhesive bonding strategy ensures reliable fluid routing while minimizing potential leakage points. Furthermore, the centrifugal force-driven microsphere generation mechanism eliminates the need for complex pump systems and precise flow control equipment, significantly reducing operational complexity and cost.

The biological performance of our microspheres demonstrates the system's utility for advanced tissue engineering applications. The particles effectively support both traditional cell encapsulation and innovative spheroid formation approaches. Transcriptomic analysis reveals that these microsphere-induced spheroids exhibit enhanced adipogenic potential, suggesting broader applications in directed cell differentiation and tissue modeling. The observed upregulation of key adipogenic markers (Pparg, Fabp4, and Adipoq) provides molecular validation of the system's effectiveness.

Looking forward, this platform offers several promising directions for future development. The current design could be adapted for producing microspheres with different material compositions, potentially enabling the creation of more complex tissue-mimetic structures. Integration of additional functional elements, such as sorting or collection chambers, could further enhance the system's capabilities. The simplified operation and high throughput make this approach particularly suitable for scaling up production for larger-scale tissue engineering applications.

Conclusion

In conclusion, our centrifugal microfluidic platform represents a significant advancement in microsphere production technology, offering a robust, simplified approach for generating highly uniform and biocompatible cell culture scaffolds. The system's technical advantages – including oil-free operation, precise size control, parallel processing capability, and simplified fabrication – make it a valuable tool for various biomedical applications, from fundamental research to potential therapeutic developments.

Data availability

The data that support the findings of this study are available from the corresponding author upon reasonable request.

Author contributions

Conceptualization: Yiwei Li; methodology: Yiwei Li, Xueqing Ren, Xin Wang, Xiaolu Cai, and Yi Zou; investigation: Yiwei Li, Xueqing Ren, Xin Wang, and Xiaolu Cai; visualization: Yiwei Li and Xueqing Ren; funding acquisition: Yiwei Li and Bi-Feng Liu; project administration: Yiwei Li; supervision: Yiwei Li, Bi-Feng Liu, and Peng Chen; writing – original draft: Yiwei Li and Xueqing Ren; writing – review & editing: Yiwei Li, Bi-Feng Liu, and Peng Chen.

Conflicts of interest

There are no financial conflicts of interest related to this study.

Acknowledgements

Yiwei Li and Bi-Feng Liu gratefully acknowledge the financial support from the National Key Research and Development Program of China (2024YFF1207300 and 2023YFF1205002), the National Natural Science Foundation of China (Grant numbers 32171248, 12472319, 22074047, 21775049, 31700746, and 82170883), and the Fundamental Research Funds for Central Universities, HUST (2021GCRC056). We are also grateful to the Core Facilities of Life Sciences, Huazhong University of Science and Technology for support, especially for the technical assistance from B. Liu, M. Lei, Y. Luo, and Y. Yi.

References

1 Z. Zhao, Z. Wang, G. Li, Z. Cai, J. Wu, L. Wang, L. Deng, M. Cai and W. Cui, *Adv. Funct. Mater.*, 2021, **31**, 2103339.
2 L. Huang, A. M. E. Abdalla, L. Xiao and G. Yang, *Int. J. Mol. Sci.*, 2020, **21**, 1895.
3 A. K.-L. Chen, S. Reuveny and S. K. W. Oh, *Biotechnol. Adv.*, 2013, **31**, 1032–1046.
4 B. Li, L. Zhang, Y. Yin, A. Chen, B. R. Seo, J. Lou, D. J. Mooney and D. A. Weitz, *Matter*, 2024, **7**, 3447–3468.
5 O. Hasturk, J. A. Smiley, M. Arnett, J. K. Sahoo, C. Staii and D. L. Kaplan, *Adv. Healthcare Mater.*, 2022, **11**, 2200293.
6 Y. Morimoto, M. Onuki and S. Takeuchi, *Adv. Healthcare Mater.*, 2017, **6**, 1601375.
7 A. Kumachev, J. Greener, E. Tumarkin, E. Eiser, P. W. Zandstra and E. Kumacheva, *Biomaterials*, 2011, **32**, 1477–1483.
8 P. Panda, S. Ali, E. Lo, B. G. Chung, T. A. Hatton, A. Khademhosseini and P. S. Doyle, *Lab Chip*, 2008, **8**, 1056.
9 H. Zimmermann, S. G. Shirley and U. Zimmermann, *Curr. Diabetes Rep.*, 2007, **7**, 314–320.
10 A. D. Augst, H. J. Kong and D. J. Mooney, *Macromol. Biosci.*, 2006, **6**, 623–633.
11 X. Duan and H. Sheardown, *Biomaterials*, 2006, **27**, 4608–4617.
12 Y. T. Matsunaga, Y. Morimoto and S. Takeuchi, *Adv. Mater.*, 2011, **23**(12), H90–H94.
13 A. Partovinia and E. Vatankhah, *Carbohydr. Polym.*, 2019, **209**, 389–399.
14 S. M. Naqvi, S. Vedicherla, J. Gansau, T. McIntyre, M. Doherty and C. T. Buckley, *Adv. Mater.*, 2016, **28**, 5662–5671.
15 C. L. Franco, J. Price and J. L. West, *Acta Biomater.*, 2011, **7**, 3267–3276.
16 P. Qi, R. Bu, H. Zhang, J. Yin, J. Chen, A. Zhang, J. Gou, T. Yin, Y. Zhang, H. He, P. Wang, X. Tang and Y. Wang, *Mol. Pharmaceutics*, 2019, **16**, 3502–3513.
17 Q. Zhao, H. Cui, Y. Wang and X. Du, *Small*, 2020, **16**, 1903798.
18 D. Lee, M. Jang and J. Park, *Biotechnol. J.*, 2014, **9**, 1233–1240.
19 Y. Deng, N. Zhang, L. Zhao, X. Yu, X. Ji, W. Liu, S. Guo, K. Liu and X.-Z. Zhao, *Lab Chip*, 2011, **11**, 4117.
20 S.-M. Kang, G.-W. Lee and Y. S. Huh, *Sci. Rep.*, 2019, **9**, 12776.
21 M. Liu, X.-T. Sun, C.-G. Yang and Z.-R. Xu, *J. Colloid Interface Sci.*, 2016, **466**, 20–27.
22 Z. T. F. Yu, J. G. Joseph, S. X. Liu, M. K. Cheung, P. J. Haffey, K. Kurabayashi and J. Fu, *Sens. Actuators, B*, 2017, **245**, 1050–1061.
23 S. Yang, S.-H. Kim, A. Intisar, H. Y. Shin, H. G. Kang, M. Y. Kim, J. M. Kim, H. R. Roh, S. Y. Oh, S.-Y. Kong, Y. Z. Kim, J. Y. Joung and M. S. Kim, *Anal. Chem.*, 2023, **95**, 9949–9958.
24 Z. Tang, F. Lv, D. E. Reynolds, S. Zhang, S. Zheng, J. Ko, Y. Chen and Y. Wang, *Lab Chip*, 2023, **23**, 2758–2765.
25 Z. Chen, P. Liao, F. Zhang, M. Jiang, Y. Zhu and Y. Huang, *Lab Chip*, 2017, **17**, 235–240.
26 C. Wei, C. Yu, S. Li, J. Meng, T. Li, J. Cheng, F. Pan and J. Li, *Anal. Chem.*, 2022, **94**, 3939–3947.
27 Y. Xiao, M. Zhou, C. Liu, S. Gao, C. Wan, S. Li, C. Dai, W. Du, X. Feng, Y. Li, P. Chen and B.-F. Liu, *Biosens. Bioelectron.*, 2024, **255**, 116240.
28 H. Yuan, C. Wan, X. Wang, S. Li, H. Xie, C. Qian, W. Du, X. Feng, Y. Li, P. Chen and B. Liu, *Small*, 2024, **20**, 2310206.
29 Y. Wan, M. Zhang, Z. Liu, B. Wang, Y. Liu, P. Chen, Y. Li, W. Du, X. Feng and B.-F. Liu, *Talanta*, 2025, **282**, 126959.
30 X. Wang, X. Cai, C. Wan, H. Yuan, S. Li, Y. Zhang, R. Zhao, Y. Qin, Y. Li, B. Liu and P. Chen, *Adv. Sci.*, 2025, **12**, 2411459.
31 Q. He, J. Zhang, Y. Liao, E. V. Alakpa, V. Bunpetch, J. Zhang and H. Ouyang, *Biotechnol. Adv.*, 2020, **39**, 107459.
32 W. Chen and Y. W. Tong, *Acta Biomater.*, 2012, **8**, 540–548.
33 M. Chen, X. Wang, Z. Ye, Y. Zhang, Y. Zhou and W.-S. Tan, *Biomaterials*, 2011, **32**, 7532–7542.
34 R. A. Perez, A. El-Fiqi, J.-H. Park, T.-H. Kim, J.-H. Kim and H.-W. Kim, *Acta Biomater.*, 2014, **10**, 520–530.
35 D. Qian and A. Lawal, *Chem. Eng. Sci.*, 2006, **61**, 7609–7625.
36 P. Sobieszuk, P. Cygański and R. Pohorecki, *Chem. Eng. Res. Des.*, 2010, **88**, 263–269.
37 I. L. Chaves, L. C. Duarte, W. K. T. Coltro and D. A. Santos, *Chem. Eng. Res. Des.*, 2020, **161**, 260–270.
38 Q. He, Y. Liao, J. Zhang, X. Yao, W. Zhou, Y. Hong and H. Ouyang, *Small*, 2020, **16**, 1906539.
39 D. Moseti, A. Regassa and W.-K. Kim, *Int. J. Mol. Sci.*, 2016, **17**, 124.
40 M. A. Ambele, P. Dhanraj, R. Giles and M. S. Pepper, *Int. J. Mol. Sci.*, 2020, **21**, 4283.
41 R. Li, J. Liang, S. Ni, T. Zhou, X. Qing, H. Li, W. He, J. Chen, F. Li, Q. Zhuang, B. Qin, J. Xu, W. Li, J. Yang, Y. Gan, D. Qin, S. Feng, H. Song, D. Yang, B. Zhang, L. Zeng, L. Lai, M. A. Esteban and D. Pei, *Cell Stem Cell*, 2010, **7**, 51–63.
42 J. G. Boucher, A. Boudreau, S. Ahmed and E. Atlas, *Environ. Health Perspect.*, 2015, **123**, 1287–1293.